Experimental and Numerical Modeling of the Stress Rupture Behavior of Nickel-Based Single Crystal Superalloys Subject to Multi-Row Film Cooling Holes

Yuanming Xu [1], Weikang Sun [1], Wei Dai [2,*], Chunyan Hu [3], Xinling Liu [3] and Weifang Zhang [2]

[1] School of Aeronautical Science and Engineering, Beihang University, Beijing 100191, China; xuymg@sina.com (Y.X.); sunweikang@buaa.edu.cn (W.S.)
[2] School of Reliability and Systems Engineering, Beihang University, Beijing 100191, China; zhangweifang@buaa.edu.cn
[3] Beijing Institute of Aeronautical Materials, Beijing 100095, China; fachcy@163.com (C.H.); liuxinling119@163.com (X.L.)
[*] Correspondence: dw@buaa.edu.cn; Tel.: +86-010-8233-8673

Abstract: The stress rupture behavior of nickel-base single crystal superalloys is a primary issue facing aero-engine design, which has been studied for more than 40 years. To a large degree, it is the existence of film cooling holes with the introduction of air cooling techniques that adds the extra challenge to the problem. Using both experimental and numerical methods, we explore here the stress rupture behavior of nickel base single crystal plate specimens subject to multi-row film cooling holes. As the numerical simulation part, finite element analysis using Abaqus was performed. Numerical results reveal that the existence of film-holes causes stress concentration and transforms local stress from uniaxial to multi-axial. For the stress distribution of different types of specimens, we defined a stress multiaxiality factor to quantitatively characterize the degree of the stress complexity and examined its effect on the rupture behaviors of the specimens along with the true stress concentration factor. The test was also carried out and results indicated that the creep rupture lives of one- and two-row specimens turn out to be longer than those of non-hole specimen. However, the three- and four-row configuration showed the opposite trend. Among the geometric parameters of film-hole configuration, film-hole row spacing is a predominant one influencing the creep rupture properties. Numerical results agree well with the fracture positions and shapes of specimens.

Keywords: single crystal; superalloy; flim cooling hole; creep rupture behavior; FEA

1. Introduction

In the past few decades, nickel-based single crystal superalloys (SXs) have been widely used in hot section components (mainly gas turbine blades) because of their excellent performance against high temperature creep. The SXs consist a two-phase microstructure including a regular embedded phase of cuboidal L12 γ' precipitates and an face-centered cubic (FCC) matrix, leading to complicated deformation mechanisms. Together with the anisotropy of SXs, and inherently complex nature of creep and dislocation motion in the γ/γ' structures, this makes it the subject of numerous scientific investigations to estimate and model the mechanical properties of single crystal superalloys.

Various models were proposed to explain the creep mechanism of single crystals and to predict the creep rupture lives. In earlier works, the elastic-plastic constitutive relationships developed since the 1960s are strain rate independent [1–4]. Later, a viscoplastic approach was proposed to gain unique solutions [5–7]. Based on such plastic constitutive frame and the damage mechanics, many other models with different damage parameters were proposed [8–12]. Furthermore, mechanism based

models [13–15], microstructure sensitive models [16–18] and multi-scale models [19–21] have also been built in recent decades. All these models can either elucidate certain physical mechanism to a degree or predict the creep rupture lives of SXs with certain degree of accuracy.

However, there is enough experimental evidence showing that far more factors can contribute to the creep behaviors and thus the creep rupture life of SXs in practical applications. Tian [22] studied the creep behavior of SXs with different content of element Re by microstructure observation and creep test at 1060–1100 °C and 120–150 MPa, and found that alloys with 4.2 wt. % Re displays a lower strain rate during steady state creep and longer creep rupture life than alloys with 2 wt. % Re. Sass [23] conducted creep test of a second generation nickel-based single crystal named CMSX-4 at 1123 K/500 MPa, 1123 K/650 MPa and 1253 K/350 MPa, respectively, and suggested that the creep resistance declines in sequence of [001], [011] and [111] at 1123 K. However, the anisotropy between [001] and [011] is strongly reduced, although the [111] orientation remains weak at 1253 K. The decline of stacking fault energy can ameliorate the creep properties by facilitating the microtwinning process [24] and the large lattice misfit leads to denser γ/γ' interfacial dislocation network, which contributes to small minimum creep rate in the secondary creep stage [25]. Furthermore, macroscopic creep deformation and microscopic mechanisms are affected by relatively small changes in creep test conditions in SXs (CMSX-4) [26,27]. For example, the microstructure is stable below approximately 900–950 °C (depending on the specific alloy), while above these temperatures, a rafted structure of γ' platelets formed, which can either boost or deteriorate creep performance relying on the details of test conditions [28–31]. Therefore, creep behaviors and creep rupture properties are correlated with chemical composition, crystallographic orientation and microstructure of SXs as well as certain creep test conditions.

The creep of SXs as one case of the most classic problem of mechanics, except for the material and the creep test condition, geometry of the investigated structure is also a decisive factor to be concerned; however, there is very limited work focusing on this issue. The creeping behavior in the thin wall SXs structures was examined [32], and the creep response presented to be larger than in test specimens typically used to characterize the material. For the issue of stress multiaxiality caused by the notches and film-holes of specimens, a number of research works were conducted. Ref. [33] showed that the notched specimens exhibit a longer creep rupture life than the smooth specimens under the same minimum-section stress, which was the so-called notch strengthening effect. Ref. [34] studied the evolution of plasticity for SXs cooled blade using specimens with a single hole, and the results showed that the stress fields form four banded stripes around the hole, on which the initiation and propagation of the cracks are experimentally proved to be dependent. The finite element analysis (FEA) simulation was carried out by Yu [35] to investigate the creep damage evolution in a 14 film-hole specimen of SXs and the experiment revealed that the creep damage is localized in the film-holes region, where the fracture will occur easily. Ref. [36] found that specimens of SXs with different slant-angles of film-holes can exhibit different damage distributions as well as different crack propagation directions. All these indicated that local geometrical features of specimens may play a remarkable role in creep rupture properties of SXs components.

To date, most studies have focused on understanding the physical phenomena regarding the film cooling process and finding the most effective film-hole configurations with a minimal amount of coolant because film cooling techniques were widely used as an active cooling method for higher thermal efficiency in practical applications. However, little research work was done to investigate the effect of film-hole configurations on creep behavior of SXs.

The objective of this paper is to investigate the effects of multi-row film-hole configuration of a second generation nickel-based single crystal superalloy DD6, both in experimental and numerical approaches. The plate specimens with 0–4 rows of small holes of 0.3 mm diameter were used to model the air-cooled turbine blades. In addition, creep test at 980 °C/300 MPa were carried out in crystallographic orientation [001] to examine the influence of these geometric features on stress distributions and the stress rupture behavior of DD6 specimens. The fracture positions and morphology of specimens in the experiment procedure were analyzed and compared with the FEA simulation

results. Both global stress distribution of specimens and local stress state features around film-holes characterized by multiaxiality factor and maximal shear stress were presented. A discussion of the geometric configuration parameters of film-holes and their effects on the stress distribution and rupture lives were given.

2. Materials

The material used in this research is DD6, a second generation nickel-based single crystal superalloy, which is one of the promising candidate materials for aero-engine design in China. The chemical composition is given in Table 1.

Table 1. Nominal chemical compositions of DD6 alloy (in wt. %).

Co	W	Ta	Al	Cr	Re	Mo	Nb	Hf	Ni
9	8	7.5	5.6	4.3	2	2	0.5	0.1	Balance

Single crystals were provided by Beijing Institute of Aeronautical Materials (Beijing, China). All the materials tested came from cast cylindrical bars (about 80 mm in diameter), whose microstructure consists of cuboidal γ' precipitates embedded in a γ channels as marked in Figure 1 [37]. The heat treatment regime is: 1290 °C × 1 h + 1300 °C × 2 h + 1315 °C × 4 h/ air cooling (AC) + 1120 °C × 4 h/AC + 870 °C × 32 h/AC. The size of γ' particles is 400–700 nm, the volume fraction of the precipitate phase is calculated to be approximately 65% according to Ref. [38], and all the specimens are [001] oriented (disorientations were controlled below 10 degrees).
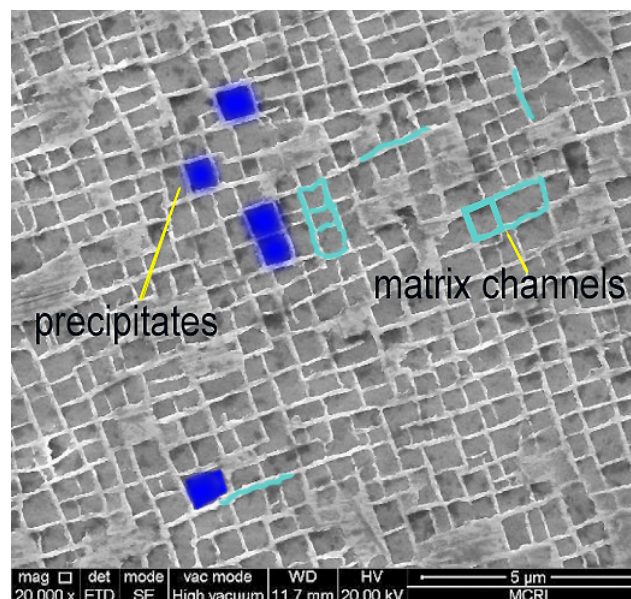

Figure 1. Microstructure of nickel based single crystal superalloys [37].

3. Methods

3.1. Experimental Setup

Plate specimens with were 0–4 rows of film-holes were designed and machined from the single crystal cast bars. As shown in Figure 2, each type of specimens has a total length of 46 mm, a uniform thickness of 1.5 mm and a gauge of 10 mm in length and 3 mm in width. The film-holes, with a radius of 0.15 mm, were punched with electro-stream machining (ESM) equipment (Beijing BAMTRI Dairui Technology Development Co., Ltd., Beijing, China). The final operation of machining was in each cases a fine grinding.

The four types of film-hole configurations are designed according to the following strategies: (1) The total number of film-holes is 10 for all specimens with film-holes (the extra two film-holes for the four-row configuration are added to even the film-hole distribution); (2) all the film-holes are as evenly distributed in the same region of the gauge area as possible.
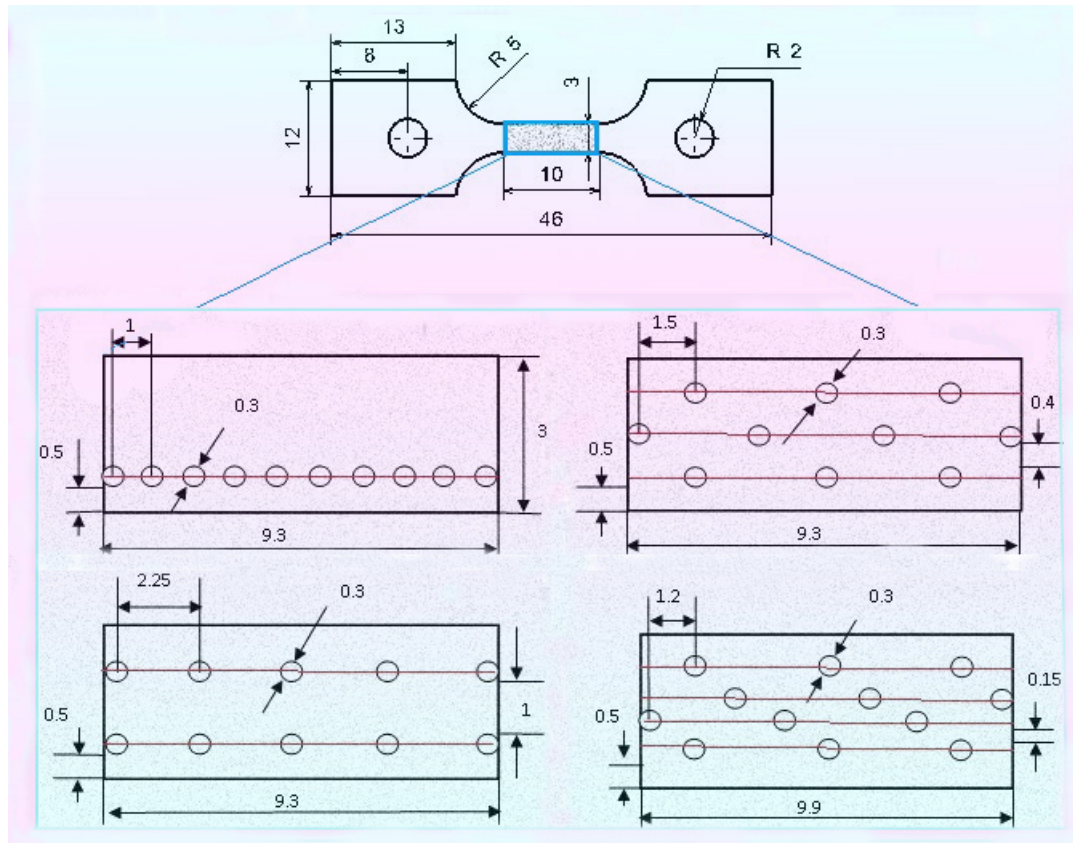

Figure 2. Diagram of the non-hole specimen and the detailed configurations of those withfilm-holes (dimension: mm).

In order to exclusively study the influence of film-hole configurations on the stress rupture behavior of the specimens, all of the stress rupture tests reported in this paper were conducted in air at a constant temperature of 980 °C under a constant load regime in tension, namely, at the same initial net section tensile stress of 300 MPa. Since the area of loading end surface is 1.5×12 mm^2, while that of net sections for zero- to four-row specimens are $1.5 \times 3 \times (1, 0.9, 0.8, 0.8, 0.8)$ mm^2, respectively, to achieve constant nominal load, specimens with 0–4 rows of film-holes were applied loads of 75 MPa, 67.5 MPa, 60 MPa, 60 MPa and 60 MPa in sequence.

3.2. Numerical Modeling

3.2.1. The Overall Procedure

Figure 3 illustrates the overall procedure of progressive simulation of the stress rupture behavior of specimens with different film-hole configurations. The full process starts with the geometrically modeling and meshing of the 0–4-row specimens. Then, material parameters (influenced by the crucial factor of microstructure), loading and boundary conditions, together with models built in the previous step were integrated into the FEA solver to obtain the stress distribution and even detailed data. The stress state can interact with the microstructure of the materials (i.e., in a way of damage evolution) and consequently has influence on the deformation and stress rupture behaviors of the specimens.

By a further data process, strain and strain rate can also be output for the prediction of rupture life and the calculation of elongation.
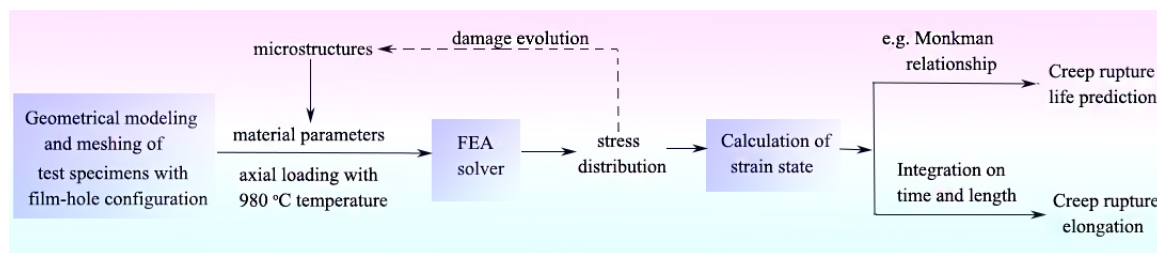

Figure 3. Progressive simulation of microstructure evolution and mechanical behavior of DD6 specimens with different film-hole configurations (FEA: Finite element analysis).

3.2.2. Constitutive Relationship

Tayler et al. [39], Rice et al. [1] and Peirce et al. [6] have laid the very foundation of the single crystal plasticity theory and constitutive relationship we use in this paper. The hypothesis used in many research works and the same here is that the creep deformation does not affect elastic deformation and then

$$\Delta\sigma = D^e \Delta\varepsilon, \tag{1}$$

where $\Delta\sigma$, $\Delta\varepsilon$ and D^e are the stress increment, the strain increment and the elastic stiffness tensor, respectively.

The transformation between the local crystallographic coordinate system ([001]-[010]-[100]) and the global coordinate system (o–x–y–z) follows the relationship:

$$D' = TDT^T, \tag{2}$$

where D' and T are the deviatoric elastic stiffness tensor and the transformation tensor, respectively.

The resolved shear stress $\tau^{(\alpha)}$ in slip system α can be determined by:

$$\tau^{(\alpha)} = \sigma : P^{(\alpha)}, \tag{3}$$

where σ is the tensor of the applied stress. In addition,

$$P^{(\alpha)} = (m^\alpha n^{\alpha^T} + m^{\alpha^T} n^\alpha), \tag{4}$$

where m^α and n^α are vectors of the normal and slipping direction corresponding to the slip system α, respectively. Three types of slip systems (namely $\{100\} < 110 >$, $\{111\} < 110 >$ and $\{111\} < 112 >$) and the relating $P^{(\alpha)}$ values are given in Supplementary Material.

Similar to the expression of the stress, the strain ε_{ij} can be evaluated with

$$\varepsilon_{ij} = \sum_{\alpha=1}^{N} \gamma^{(\alpha)} P^{(\alpha)}, \tag{5}$$

where $\gamma^{(\alpha)}$ and N are the resolved shear strain in the slip system α and the number of the activated slip system, respectively.

Norton creep constitutive relationship between the resolved shear stress and strain rate, which can describe the primary and second stages of creep deformation with satisfying accuracy, is written as the following:

$$\dot{\gamma}^{(\alpha)} = a(\tau^{(\alpha)})^n, \tag{6}$$

where $\dot{\gamma}^{(\alpha)}$, a and n are consecutively the rate of resolved shear strain and the two creep materials parameters.

This creep constitutive relationship has been implemented into the general purpose FEA software Abaqus as a user subroutine User-defined Material (UMAT) [40].

3.2.3. Meshing

Figure 4 displays the meshes of three-dimensional finite element models with completely identical geometric features compared to the specimens. C3D8R elements are used for Abaqus calculation and the meshes in the vicinity of film-holes are carefully refined. The boundary conditions and loads are shown in Figure 4. The left end surface is fixed while the right one is free from geometric constraint but applied with a uniform tensile load p_x, which takes the values of the corresponding ones as mentioned before in Section 3.1. The crystallographic orientation of the specimen is [001], which is aligned with the x-axis of x–y–z coordinate system as well as the loading direction. The material parameters mentioned in the previous section are $a = 2 \times 10^{-15} \text{ s}^{-1}/\text{MPa}^n$, $n = 5.11$ [41].
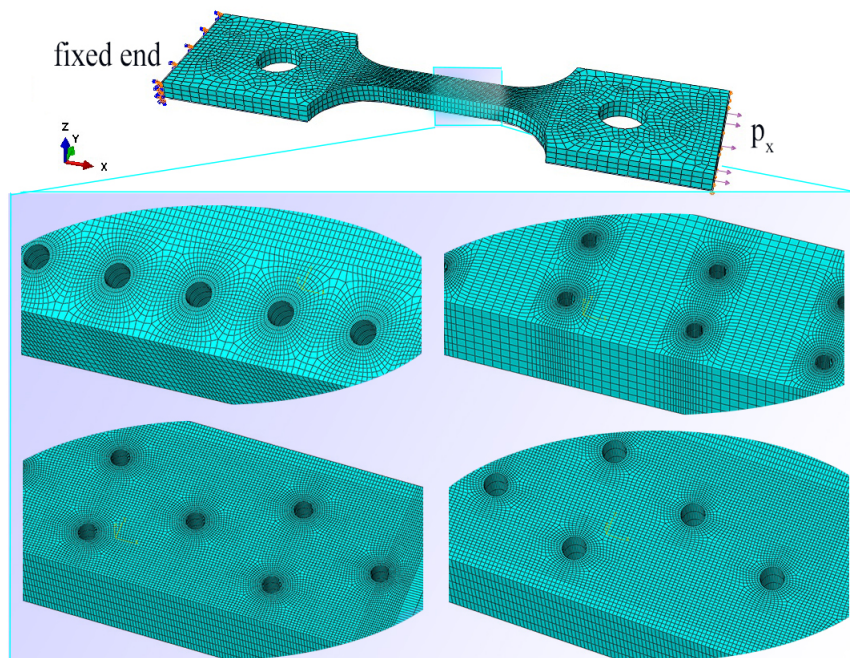

Figure 4. Finite element models of different types of specimens.
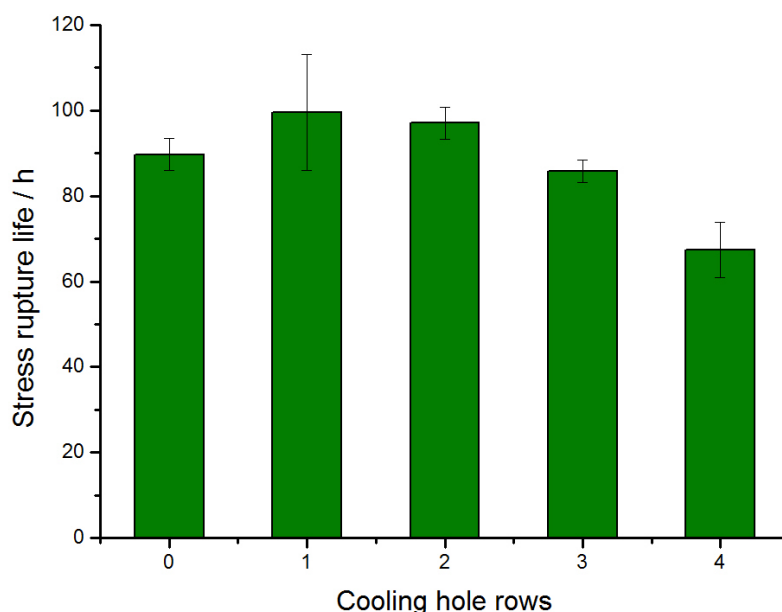
4. Results

4.1. Stress Rupture Lives of Specimens with Different Film-Hole Configurations

Table 2 gives both raw rupture life data and further statistic results of the stress rupture test regarding 27 valid specimens. As can be seen, except for rupture lives of one-row specimens, most experimental results are of sufficient confidence (over 90%) with relative deviation of 5%.

Figure 5 illustrates the film-hole configuration dependence of stress rupture lives. It can be observed that one- and two-row specimens have longer stress rupture lives than those without film-holes, which similar to "the notch strengthening effect" [33] can be called the film-hole strengthening effect. However, this strengthening effect disappears when the film-hole rows of specimens reach three or more. As far as specimens with cooling holes are concerned, stress rupture lives decrease generally with the increasing rows of the film-holes.

Table 2. Stress rupture test results of DD6 specimens.

Film-Hole Rows		0	1	2	3	4
Raw data of stress rupture life/h	NO.1	97	134	88	89	72
	NO.2	77	163	105	92	78
	NO.3	90	83	95	85	77
	NO.4	96	84	91	78	70
	NO.5	97	83	108	-	72
	NO.6	83	77	-	-	43
Statistic results	Average life/h	89.66	99.55	97.09	85.84	67.40
	Confidence level	>95%	>80%	>95%	>95%	>90%

Figure 5. Film-hole configuration dependence of the creep rupture lives.

4.2. The Global Stress Distributions of Specimens

Figure 6 presents the numerical results of the single-central-hole-plate model subjected to uni-axial tensile load, which serves as a basic model to comprehensively describe the stress distributions of 1–4-row specimens. It can be observed that the stress contour band around the central hole looks like a butterfly, namely, the butterfly-like band (B-band). The stress in the wing part (in red, yellow and green) of the "butterfly" is comparatively higher than that in the outside area of the "butterfly" while those in the head and tail part (in blue) are much lower than those outside, and this phenomenon strengthens as the B-band is confined closer to the central hole.

Numerical simulation was conducted with the method in Section 3 in order to obtain the holistic stress distribution of the specimens and meanwhile the stress state details in local areas around the film-holes. Figure 7 illustrates the stress distribution contours for both specimens with film-holes and those without after specimens undergo 10 h of creeping simulation.
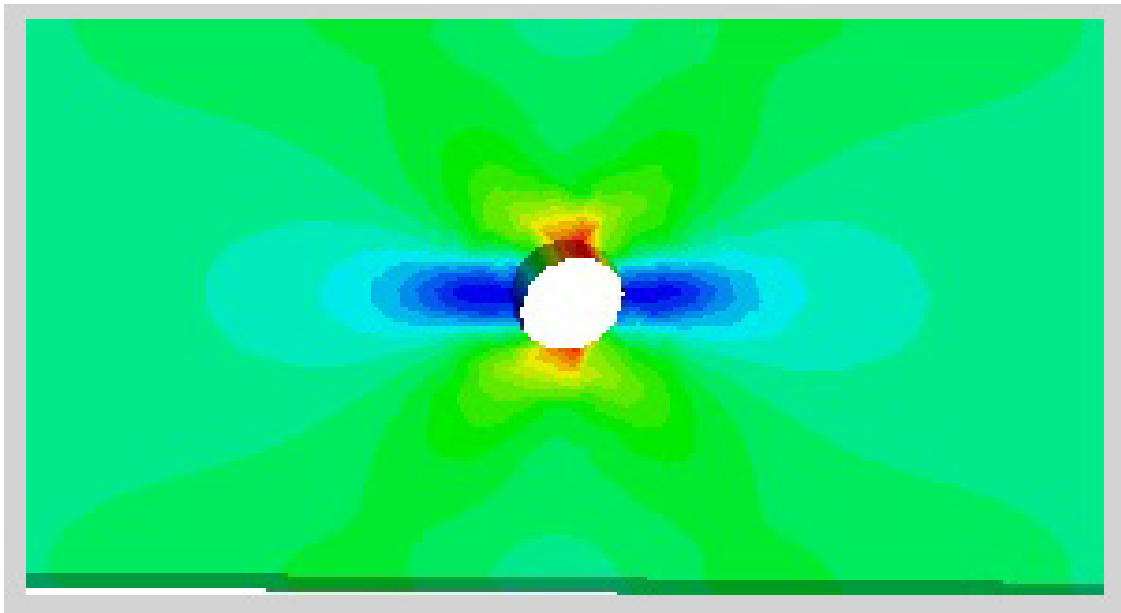
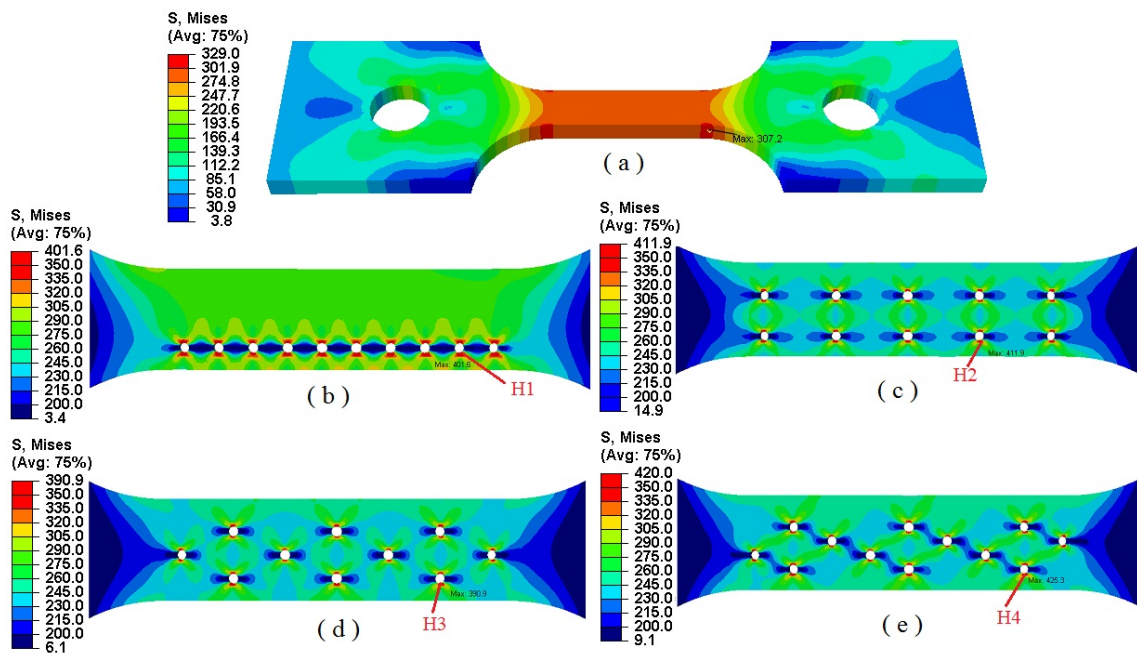**Figure 6.** Numerical results of the single-hole-plate model.

Figure 7. Stress distribution contours of specimens with different film-hole configurations: (**a**) zero-row, (**b**) one-row, (**c**) two-row, (**d**) three-row, (**e**) four-row.

For the non-hole specimen, displayed in Figure 7a, the stress outside the gauge area can be considered to have an insignificant effect on the stress rupture behavior of the specimens. Those specimens with film-holes are encountered with the similar circumstances. Therefore, only the stress distributions in the gauge areas are shown in Figure 7b–e, where the maximum Mises stresses of 1–4 row configurations are marked with H1–H4, respectively. Different from the homogeneous stress distribution in the gauge area of the non-hole specimen in Figure 7a, and similar to the case in Figure 6, B-bands (butterfly-like bands) can be observed clearly in Figure 7b–e, however, in a superimposed way at this time.

Obviously, there is a strong dependence of the stress distribution on film-hole configuration, which is featured by the distinctive intensity of the B-band-superposition in different types of specimens. As for the one-row configuration (see Figure 7b, B-bands are confined in only half of the gauge area, connected from each other in the longitudinal direction, while, in the lateral direction, keeping a comparatively large distance away from the far edge (the upper edge) .

For the two-row configuration (see Figure 7c), B-bands keep a considerable distance from each other in the longitudinal direction while connect with each other but still have a distance of two hole-diameters from the far edge in the lateral direction.

However, for the three-row configuration (see Figure 7d), both in the longitudinal and lateral direction, B-bands stay close but do not connect with each other and keep merely one hole-diameter distance from the far edge in the lateral direction.

While for the four-row configuration, Figure 7e illustrates that B-bands stay close to each other in the longitudinal direction while getting connected in every other row and already getting to the far edge in the lateral direction.

Overall, concerning specimens with different film-hole configurations, as a substantial global stress distribution feature, the intensity of stress superposition in lateral direction increases with the growth of film-hole rows.

4.3. Stress State Characterization with Principal Stresses

Recent study [37] has revealed that γ'/γ morphology changes with the stress state including the magnitude of equivalent stress, the degree of stress concentration and multiaxialiy. For example, there was regular cuboidal γ' phase without rafts for low equivalent stress (Mises stress), perfect N-type rafted structure for high equivalent stress, low stress concentration and low stress multiaxiality; however, shorter broken γ'-phase rafts for high equivalent stress, high stress concentration and high stress multiaxiality [37]. Therefore, stress state (i.e., stress concentration and multiaxialization) can have an influence on creep behavior by changing the microstructure of single crystal superalloys.

The existence of film-holes brings about two categories of effect, namely, stress concentration and stress multiaxialization , which were proved to be detrimental [35] and beneficial [33], respectively, in the sense of the "notch strengthening effect". The former can be characterized by the true stress concentration factor κ as the following equation:

$$\kappa = \frac{(\sigma_{mises})_{max}}{\sigma_0},$$ (7)

where $(\sigma_{mises})_{max}$, σ_0 are the maximum Mises stress and the true stress in most areas, respectively. Net-section stress was not used because creeping is a long term mechanical process, which is more controlled by the whole stress field in most areas than by the net-section regions. In addition, σ_{mises} can be calculated as the equation below:

$$\sigma_{mises} = \sqrt{\frac{1}{2}[(\sigma_1 - \sigma_2)^2 + (\sigma_2 - \sigma_3)^2 + (\sigma_3 - \sigma_1)^2]},$$ (8)

where σ_1, σ_2, σ_3 are the maximal principal stress, middle principal stress, and minimal principal stress, respectively.

In order to quantitatively examine the magnitude of stress complexity caused by the existence of film-holes, the stress multiaxiality factor λ is defined in this paper by the following equation:

$$\lambda = \frac{(|\sigma_1| + |\sigma_2| + |\sigma_3|) - max\{|\sigma_1|, |\sigma_2|, |\sigma_3|\}}{2(max\{|\sigma_1|, |\sigma_2|, |\sigma_3|\})},$$ (9)

where σ_1, σ_2, σ_3 are again the maximal principal stress, middle principal stress, minimal principal stress, respectively, and $max\{|\sigma_1|, |\sigma_2|, |\sigma_3|\}$ equals the maximum of $|\sigma_1|$, $|\sigma_2|$ and $|\sigma_3|$. The value of λ

ranges from 0 to 1. For example, λ takes the value of 0 for uniaxial tensile or compression stress state, 0.5 when one of the three principal stresses is zero and the other two are equal in magnitude (but can either be positive or negative) and 1 when all the three principal stresses are equal in magnitude (again can either be positive or negative).

Table 3 lists the FEA calculated stress magnitude of critical nodes (i.e., the maximal Mises stress) at the time of fracture of all the specimens. The values of two concerned factors mentioned above are also included in the table. The stress multiaxiality factor ranges from 0.234 to 0.330, whereas the true stress concentration factor is between 1.380–1.738 for specimens with film-holes. It can seen that both values are much higher than those of specimens without film-holes in the uniaxial case. It illustrates that the defined stress multiaxiality factor can reflect evidently the extent of multiaxialization of the stress distribution as a result of the local geometric features. The true stress concentration factor, similar to the traditional concentration factor, specifies the amplification effect of the stress magnitude with the existence of film-holes.

Table 3. Overall stress results of specimen with 0–4 rows of film-holes.

Hole Rows	Nominal Stress/MPa	σ_0 /MPa	σ_1/MPa	σ_2/MPa	σ_3/MPa	λ	κ
0	300	300	312.0	9.4	5.9	0.025	1.014
1	300	270	523.0	205.4	112.7	0.304	1.380
2	300	240	467.0	182.0	103.1	0.305	1.381
3	300	240	542.7	242.9	114.7	0.330	1.585
4	300	240	521.2	191.4	52.1	0.234	1.738

Simulation generally reveals that the stress concentration effect of specimens with film-holes increases with the adding rows of film-holes monotonically, while, for the stress multiaxiality factor, this is not the case. The magnitude of both factors (λ and κ) are almost the same for one- and two-row configuration, which means that the creep rupture lives of corresponding specimens should also keep the identical level approximately. This has been proved by the experiment results in Section 3.1. In addition, the comparatively high stress multiaxiality factor and low stress concentration factor explain the reason why the rupture lives in these two cases are higher than those in the non-hole case.

The stress concentration factor reaches a maximum of 1.738 at the four-row configuration, where the stress multiaxiality factor is the lowest at 0.234 among the specimens with film-holes. Given that stress concentration factor is detrimental and stress multiaxiality is beneficial [33], this accounts for why the rupture life of four-row specimens is the minimum.

The maximum value of λ 0.330 occurs in specimens with three-row configurations in which film-holes are evenly arranged with nearly the same distance from each other. However, its stress concentration factor κ equals 1.585, which is much higher than those one- and two-row specimens. The testing results (see Section 3.1) revealed that its rupture life is shorter than those of one-, two- and even zero-row specimens, which implies that the true stress concentration factor κ is the dominant factor in this critical case. In other words, the extra benefit brought by the increment of stress multiaxialiy factor at this time can no longer compensate for the loss acclaimed by the increment of true stress concentration factor; therefore, the rupture life in this case lags behind the non-hole one. The research in this paper seems to give the view point that the true concentration factor is dominant for the stress rupture life of specimens and the stress multiaxiality factor also plays an influential role, meaning that when the true stress concentration factor is low while the stress multiaxiality factor is large, the rupture life may not be longer.

Figure 8 shows the time dependence of λ and κ concerning different film-hole configurations. It can be observed that, for all types of specimens, λ increases rapidly at the primary stage, but the increasing trend slows down very soon, while κ shows the exactly opposite trend, and the transient stage for both of them lasts for the same period of time (about 5 h). The stress multiaxiality λs for one-, two- and three-row configurations stay close to each other in quantity; however, λ is much lower for four-row configurations. In contrast, the true stress concentration factor κ is maximal for the four-row

configuration, followed by the three-row one and achieves the minimum value for one- and two-row configurations (which are almost identical to each other).
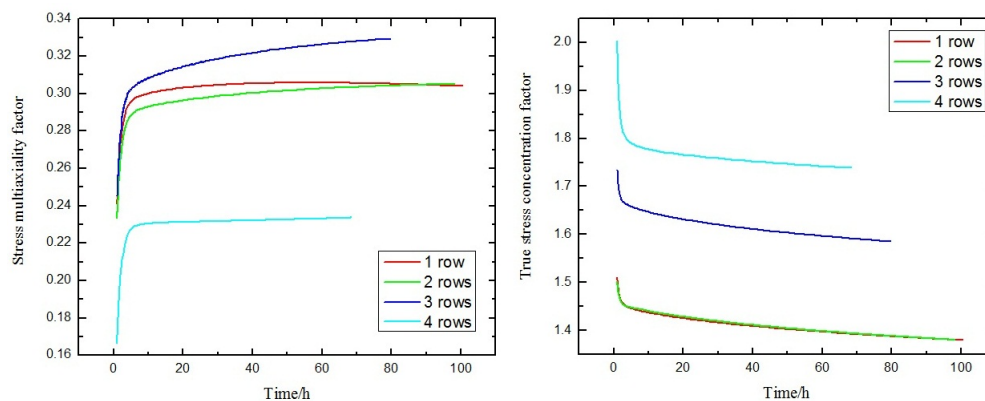

Figure 8. Time dependence of stress multiaxiality factor λ and true stress concentration factor κ.

4.4. Maximal Resolved Shear Stress

Resolved shear stress, the motive factor of the crystals' slipping process, has been proved to be a powerful tool for the analysis of physical mechanisms of the creeping process. Therefore, it is necessary to investigate the maximal resolved shear stresses in the vicinity of the film-holes. However, before that, it is important to give a big map of the slip systems, which is the very foundation of the concept of the resolved shear stress.

Figure 9 exemplifies some of the many possible slip faces (in different color) and directions (marked by arrows) of the three types of slip systems, respectively. In fact, $\{100\} < 110 >$, $\{111\} < 110 >$ and $\{111\} < 112 >$ type slip system have six, eight and eight possible slip faces and six, twelve and twelve slip directions, respectively.

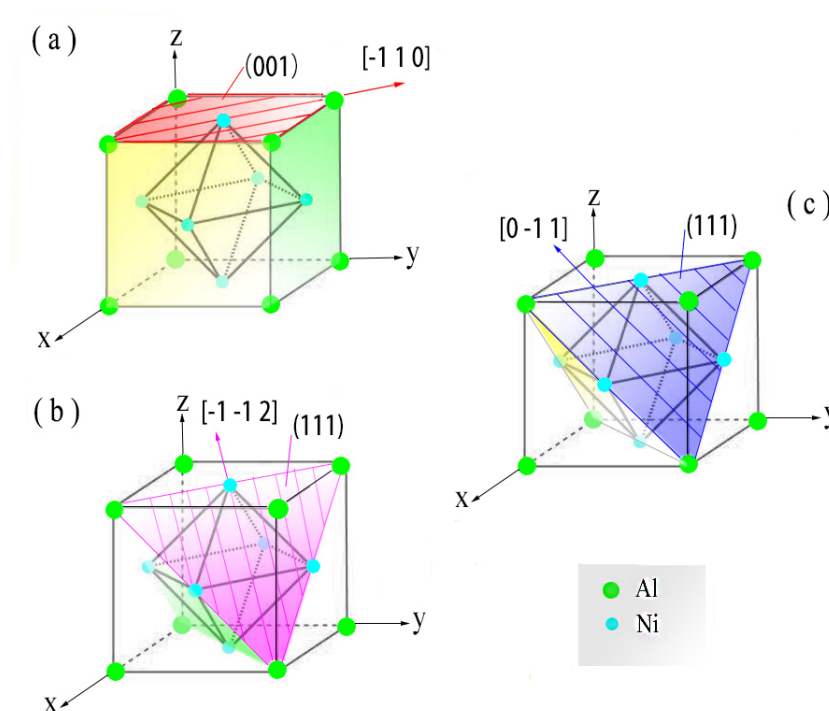**Figure 9.** Slip systems illustration of the Ni_3Al γ' precipitates: (**a**) $\{100\} < 110 >$ type slip system; (**b**) $\{111\} < 110 >$ type slip system; (**c**) $\{111\} < 112 >$ type slip system.

Figure 10 illustrates the numerical results of the maximal resolved shear stress (among the six, twelve and twelve possible ones for the three types, respectively) at the edge of the critical film-hole (where the Mises stress reaches the maximum) of the specimens with different film-hole configurations.

As can be observed, the maximal resolved shear stress distribution around the film-hole exhibits an approximate symmetry to the *x*-coordinate axis and the *y*-coordinate axis for the $\{111\} < 110 >$ type and the $\{111\} < 112 >$ type slip systems. However, there seems to be no symmetry for that of the $\{100\} < 110 >$ type slip system.

The maximal resolved shear stress of the $\{111\} < 112 >$ type slip system peaks just over 180 MPa when θ is about 90° or 270° for 1–4-row specimens; that of the $\{111\} < 110 >$ type slip system peaks around 160 MPa again when θ is about 90° or 270° for 1–4-row specimens; while that of the $\{100\} < 110 >$ type slip system peaks just about 90 MPa when θ is about 120° or 300° for 1–2-row specimens as shown in Figure 7a,b, and about 60°, 120° or 300° for 3–4-row specimens as shown in Figure 7c,d.

Therefore, the $\{111\} < 110 >$ and $\{111\} < 112 >$ type slip systems can be the main types of activated slip systems and the cracks due to creeping process may occur at the film-hole edge, where θ is 90° or 270°, which has been proved by the fracture morphology in Figure 11b–e given in Section 4.5.
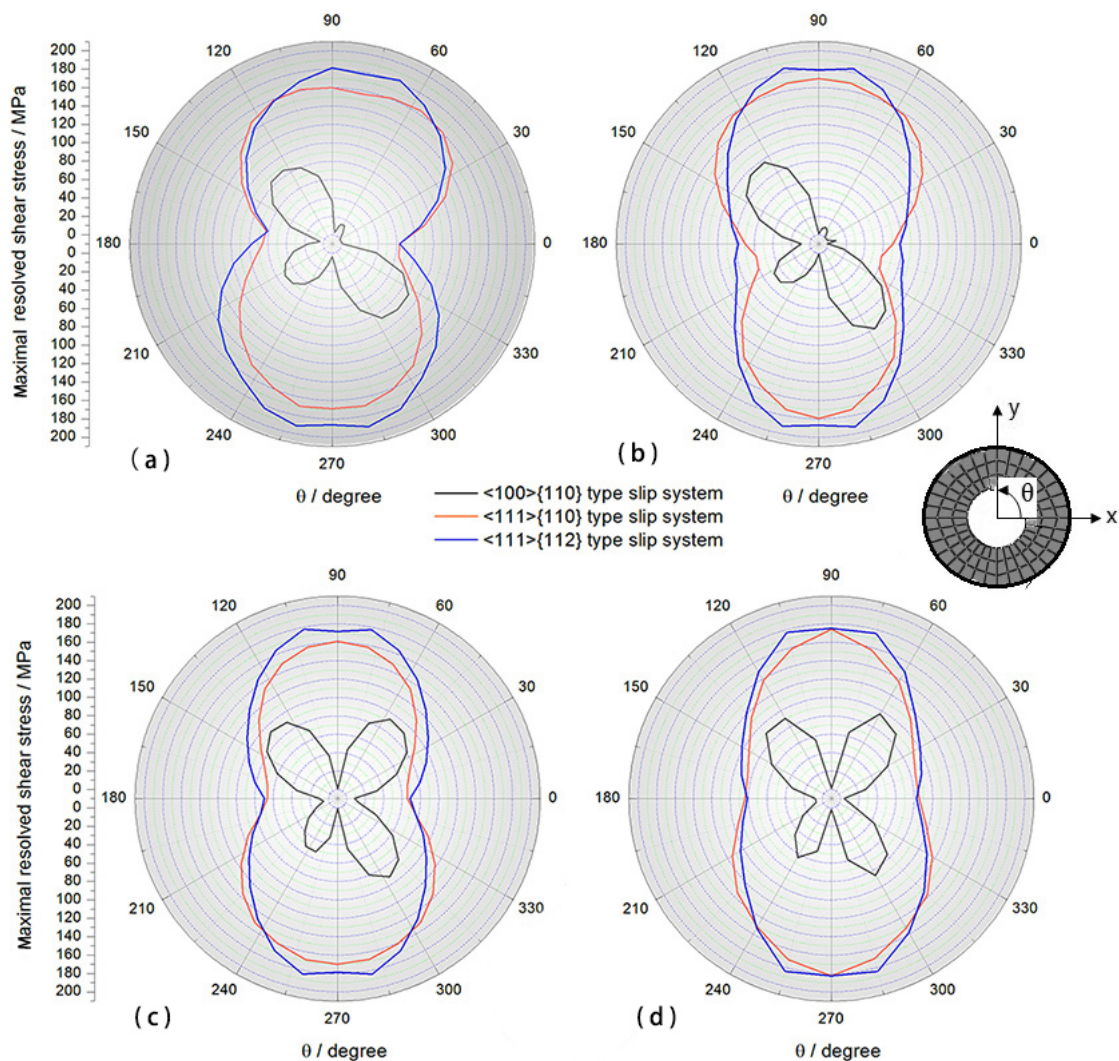

Figure 10. Numerical results of the maximal resolved shear stress at the edge of different film-holes shown in Figure 7: (**a**) H1; (**b**) H2; (**c**) H3; (**d**) H4.

4.5. Comparison between Simulation and Test on Rupture Positions and Shapes

Both the rupture morphology of the specimens and the corresponding local stress contours are given in Figure 11. It can be seen that the fracture surfaces are generally perpendicular to the loading axis for all of the specimens. However, for specimens without film-holes, the fracture occurred at one side of the gauge area while for those with film-holes, the fractures go through the film-holes in the second or third columns (counting from the loading end) for one-row configurations, the first or second columns for two-row ones and the second column for both 3–4-row configurations. In comparison with these outcomes, the numerical results (see Section 4.2) show that critical points of the specimens are located on one side of the gauge area for non-row specimens and the second column for the 1–4-row ones, which is in good agreement with the test results in terms of rupture positions.

It has been proved by engineering applications that fractures often initiate in the vicinity of critical points at a part where the stresses are higher the allowed ones. In this context, B-bands, which indicate the high stress areas around the critical points, are connected with smoothly curved lines to predict the possible fracture track, as marked in Figure 11. As can be seen, not only the rupture positions, but also the experimental fracture shapes are consistent with the numerical results to a large degree.
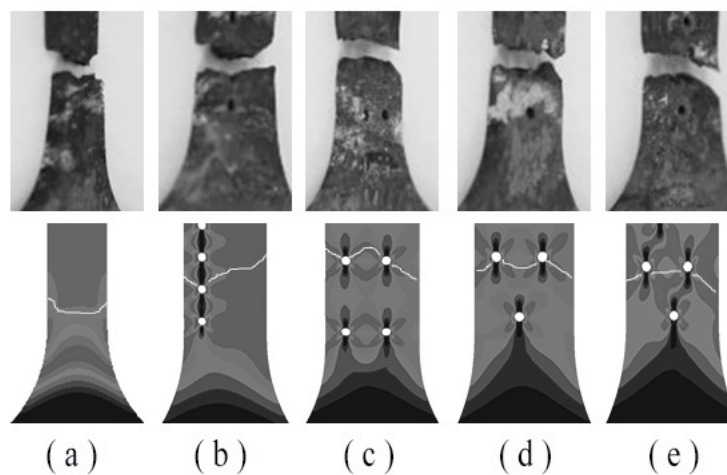

Figure 11. Comparisons between test and numerical results on fracture positions and shapes of specimens with different film-hole configurations: (**a**) zero-row, (**b**) one-row, (**c**) two-row, (**d**) three-row, (**e**) four-row.

5. Discussion

5.1. Stress Rupture Behavior

Both the experimental and numerical results described above have indicated that film-hole configuration can have a great influence on the stress rupture behavior of specimens and revealed that the stress state varies greatly with the introduction of film-holes.

It is well known that the very clue of the macroscopic mechanical properties for a specific material can generally be found by looking into its microscopic tissues. Meanwhile, considering the recent proof that stress states can influence the microstructure of a material, it can be easily inspired to bridge the film-hole configuration with the stress rupture behavior by two agents, namely, specimen stress state and materials' microstructure.

In this paper, the first bridging agent, specimen stress state, has been characterized with two effect-contradictive factors, namely the stress multiaxiality factor and the true stress concentration factor. Although stress contours have shown the stress distributions in the global sense, values of the two factors quantitatively indicate the degrees of stress concentration and stress multiaxialization in crucial local areas.

In general, the true stress concentration factor is the dominant one, the rising of which is responsible for the decrease of stress rupture lives from one- to four-row configurations. However, the introduction of the stress concentration effect by film-holes does not have to shorten the rupture lives; for example, when it is low and the stress multiaxiality factor is relatively high, the rupture life can be higher than the non-hole specimens as shown by the one- and two-row life results. However, when the true stress concentration factor further increases, the extra benefit brought by the increment of stress multiaxialiy factor, even when it is at a maximum among the four configurations at this time, can no longer compensate for the loss acclaimed by the increment of the former, which explains why the rupture lives of three- and four-row specimens lag behind the non-hole one.

It is not difficult to understand why the stress concentration factor is a detrimental one to many materials and structures, since many failures due to voids in engineering materials have proved that. However, it requires a lot of further research work to figure out why the stress multiaxiality factor can play a beneficial role such as the 'notch strengthening effect' on creep behavior of CMSX-4 superalloy single crystals [33].

Since the resolved shear stress serves as a motivating factor driving the slipping process of single crystals, one possible explanation is that transformations of the local stress distributions from uni-axial to multi-axial may result in simultaneous activation of different oriented slips of single crystals, which leads to the intersection of slip systems, stronger constraints of plastic deformation [11], falling of creep strain rate, and finally prolonged rupture lives.

5.2. Discussion on the Effects of Film-Hole Configuration

Film-hole configuration parameters (shown in Figure 12) and their possible effects on stress distribution and stress rupture lives are discussed and summarized in this section.
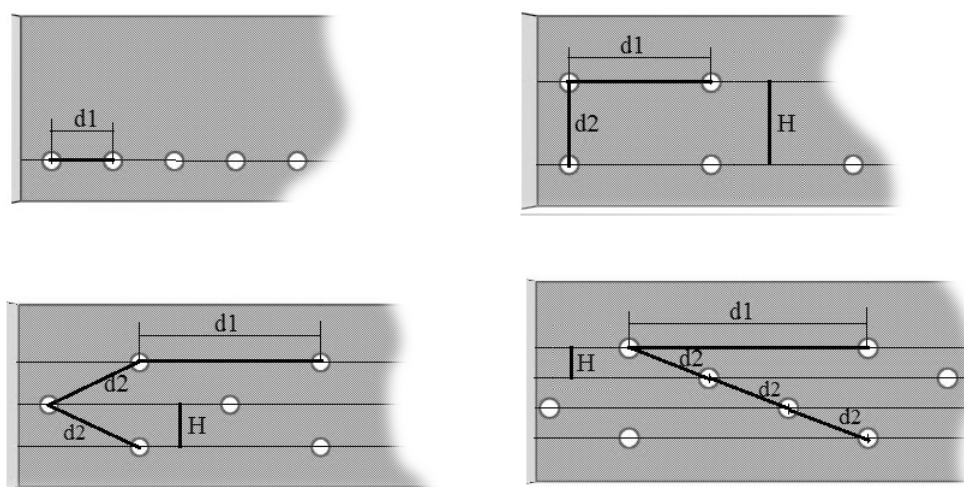

Figure 12. Diagrams of film-hole configuration and its main parameters.

The detailed data for film-hole configurations are shown in Table 4, where $d1$ denotes the spacing between film-holes in the same row, $d2$, the smallest distance between two film-holes in neighboring rows, and H, the spacing between film-hole rows. It is easy to understand that the increasing of the film-hole rows leads to the falling of H and the rising of $d1$ since the film-hole designing areas are almost the same for all types of specimens. However, the changing mode of $d2$ can be rather complicated.

Although there is no clear relationship between the configuration parameters and the stress rupture lives of the corresponding specimens, quite interestingly, the changing trend of the true stress concentration factor coincides with that of the parameter $d1$, and there is a similar trend between the stress multiaxiality factor and the parameter $d2$, when comparing the figures in Table 3 of Section 4.3 and the above table. Therefore, the number of film-hole rows (characterized by the parameter H

or *d*1) has an effect on the stress rupture life, probably by increasing the stress concentration factor, while *d*2 has an effect on the stress rupture life probably by increasing the stress multiaxiality factor. In addition, how the two factors have an influence on stress rupture behavior has been discussed before in Section 4.3 Relating to the dominant effect of the true stress concentration factor, *H* (or *d*1) can probably be the major parameter influencing stress rupture lives.

Table 4. Main film-hole configuration parameters of DD6 specimens.

Hole Rows	Main Parameters/mm		
	*d*1	*d*2	*H*
1	1	-	-
2	2.25	1.3	1.3
3	3	1.655	0.7
4	3.6	1.282	0.45

6. Conclusions

DD6 single crystal superalloy turbine blades were modelled by plate specimens subject to multi-row film-holes. A stress rupture test was carried out under 980 °C/300 MPa and numerical simulations were implemented with the finite element method.

One- and two-row specimens exhibit longer high temperature stress rupture lives than those without film-holes. However, with the increasing of film-hole rows from one to four, the creep rupture lives decrease gradually from 99.55 h to 67.40 h.

The existence of film-holes causes stress concentration and changes local stress from uniaxial to multi-axial, which was quantitatively characterized by the true stress concentration factor κ and the stress multiaxiality factor λ. Calculation of critical points reveal that κ increase with the growth of film-hole rows while λ increases first and peaks at three-row configurations. Both of them show transient changes at first, which slows down after the specimens' creeping for about 5 h.

Numerical results show that $\{111\} < 110 >$ and $\{111\} < 112 >$ type slip systems are the dominant ones among the three types of slip systems.

Among the geometric parameters of film-hole configurations, film-hole row spacing is a predominant one influencing the stress rupture properties.

Both the rupture positions and fracture morphology of specimens subject to film-holes coincide with the numerical results.

Author Contributions: Yuanming Xu and Xinling Liu conceived and designed the experiment; Chunyan Hu and Xinling Liu performed the experiment; Wei Dai and Weifang Zhang contributed analysis tools; Wei Dai, Yuanming Xu and Weikang Sun analyzed the data and wrote the paper.

Conflicts of Interest: The authors declare no conflict of interest.

References

1. Asaro, R.J.; Rice, J. Strain localization in ductile single crystals. *J. Mech. Phys. Solids* **1977**, *25*, 309–338.
2. Hill, R. Generalized constitutive relations for incremental deformation of metal crystals by multislip. *J. Mech. Phys. Solids* **1966**, *14*, 95–102.
3. Mandel, J. Generalisation de la theorie de plasticite de WT koiter. *Int. J. Solids Struct.* **1965**, *1*, 273–295.
4. Simo, J.C.; Taylor, R.L. Consistent tangent operators for rate-independent elastoplasticity. *Comput. Methods Appl. Mech. Eng.* **1985**, *48*, 101–118.
5. Asaro, R.J.; Needleman, A. Texture development and strain hardening in rate dependent polycrystals. *Acta Metall.* **1985**, *33*, 923–953.

6.   Peirce, D.; Asaro, R.J.; Needleman, A. An analysis of nonuniform and localized deformation in ductile single crystals. *Acta Metall.* **1982**, *30*, 1087–1119.

7.   Hutchinson, J. Bounds and self-consistent estimates for creep of polycrystalline materials. *Proc. R. Soc. Lond. Ser. A* **1976**, *348*, 101–127.

8.   Qi, W.; Bertram, A. Anisotropic continuum damage modeling for single crystals at high temperatures. *Int. J. Plast.* **1999**, *15*, 1197–1215.

9.   MacLachlan, D.W.; Wright, L.W.; Gunturi, S.; Knowles, D.M. Constitutive modelling of anisotropic creepdeformation in single crystal blade alloysSRR99 and CMSX-4. *Int. J. Plast.* **2001**, *17*, 441–467.

10. MacLachlan, D.W.; Knowles, D.M. Modelling and prediction of the stress rupture behaviour of single crystal superalloys. *Mater. Sci. Eng. A* **2001**, *302*, 275–285.

11. MacLachlan, D.W.; Gunturi, G.S.K.; Knowles, D.M. Modelling the uniaxial creep anisotropy of nickel base single crystal superalloys CMSX-4 and RR2000 at 1023 K using a slip system based finite element approach. *Comput. Mater. Sci.* **2002**, *25*, 129–141.

12. Xu, B.X.; Wang, X.M.; Zhao, B.; Yue, Z.F. Study of crystallographic creep parameters of nickel-based single crystal superalloys by indentation method. *Mater. Sci. Eng. A* **2008**, *478*, 187–194.

13. Svoboda, J.; Lukas, P. Model of creep in 001 oriented superalloy single crystals. *Acta Mater.* **1998**, *46*, 925–953.

14. Svoboda, J.; Lukas, P. Creep deformation modelling of superalloy single crystals. *Acta Mater.* **2000**, *48*, 2519–2528.

15. Ma, A.; Dye, D.; Reed, R.C. A model for the creep deformation behaviour of single-crystal superalloy CMSX-4. *Acta Mater.* **2008**, *56*, 1657–1670.

16. Zhu, Z.; Basoalto, H.; Warnken, N.; Reed, R.C. A model for the creep deformation behaviour of nickel-based single crystal superalloys. *Acta Mater.* **2012**, *60*, 4888–4900.

17. MacKay, R.A.; Gabb, T.P.; Nathal, M.V. Microstructure-sensitive creep models for nickel-base superalloy single crystals. *Mater. Sci. Eng. A* **2013**, *582*, 397–408.

18. Graverend, J.B.L.; Cormier, J.; Gallerneau, F.; Villechaise, P.; Kruch, S.; Mendez, J. A microstructure-sensitive constitutive modeling of the inelastic behavior of single crystal nickel-based superalloys at very high temperature. *Int. J. Plast.* **2014**, *59*, 55–83.

19. Zhou, C.; Beyerlein, I.J.; LeSar, R. Plastic deformation mechanisms of fcc single crystals at small scales. *Acta Mater.* **2011**, *59*, 7673–7682.

20. Keshavarz, S.; Ghosh, S. Multi-scale crystal plasticity finite element model approach to modeling nickel-based superalloys. *Acta Mater.* **2013**, *61*, 6549–6561.

21. Mukherjee, S.; Zhou, B.; Dasgupta, A.; Bieler, T.R. Multiscale modeling of the anisotropic transient creep response of heterogeneous single crystal SnAgCu solder. *Int. J. Plast.* **2016**, *78*, 1–25.

22. Tian, S.; Su, Y.; Qian, B.; Yu, X.; Liang, F.; Li, A. Creep behavior of a single crystal nickel-based superalloy containing 4.2% Re. *Mater. Des.* **2012**, *37*, 236–242.

23. Sass, V.; Glatzel, U.; Feller-Kniepmeier, M. Anisotropic creep properties of the nickel base superalloy CMSX-4. *Acta Mater.* **1996**, *44*, 1967–1977.

24. Tian, C.; Han, G.; Cui, C.; Sun, X. Effects of stacking fault energy on the creep behaviors of Ni-base superalloy. *Mater. Des.* **2014**, *64*, 316–323.

25. Zhang, J.; Wang, J.; Harada, H.; Koizumi, Y. The effect of lattice misfit on the dislocation motion in superalloys during high-temperature low-stress creep. *Acta Mater.* **2005**, *53*, 4623–4633.

26. MacLachlan, D.W.; Williams, S.; Knowles, D.M. Damage Mechanics Approach to Stress Rupture and Creep of Single Crystal Blade Alloys. In Proceedings of the Seventh International Conference on Creep and Fracture of Engineering Materials and Structures (TMS), Warrendale, PA, USA, 1997; p. 707.

27. MacLachlan, D.W.; Knowles, D.M. Creep-behavior modeling of the single-crystal superalloy CMSX-4. *Metall. Mater. Trans. A* **2000**, *31*, 1401–1411.

28. Pearson, D.D.; Lemkey, F.D.; Kear, B.H. Stress Coarsening of γ′ and Its Influence on Creep Properties of a Single Crystal Superalloy. In *Superalloys*; ASM: Materials Park, OH, USA, 1980; pp. 513–520.

29. Schneider, W.; Hammer, J.; Mughrabi, H. Creep Deformation and Rupture Behaviour of the Monocrystalline Superalloy CMSX-4: A Comparison with the Alloy SRR 99. In *Superalloys*; The Minerals, Metals & Materials Society (TMS): Warrendale, PA, USA, 1992; pp. 589–598.

30. Hammer, J.; Mughrabi, H. High-Temperature Creep and Microstructure of the Monocrystalline Nickel-base Superalloy SRR 99. In Proceedings of the Advanced Materials and Processes, European Conference on Advanced Materials and Processes (EUROMAT89), DGM, Oberursel, Germany, 22–24 October 1989; p. 445.

31. Caron, P.; Henderson, P.J.; Khan, T.; McLean, M. On the effects of heat treatments on the creep behaviour of a single crystal superalloy. *Scr. Metall.* **1986**, *20*, 875–880.

32. Cassenti, B.; Staroselsky, A. The effect of thickness on the creep response of thin-wall single crystal components. *Mater. Sci. Eng. A* **2009**, *508*, 183–189.

33. Lukas, P.; Preclik, P.; Cadek, J. Notch effects on creep behaviour of CMSX-4 superalloy single crystals. *Mater. Sci. Eng. A* **2001**, *298*, 84–89.

34. Mao, H.Z.; Wen, Z.X.; Yue, Z.F.; Wang, B.Z. The evolution of plasticity for nickel-base single crystal cooled blade with film cooling holes. *Mater. Sci. Eng. A* **2013**, *587*, 79–84.

35. Yu, Q.M.; Yue, Z.F.; Wen, Z.X. Creep damage evolution in a modeling specimen of nickel-based single crystal superalloys air-cooled blades. *Mater. Sci. Eng. A* **2008**, *477*, 319–327.

36. Liang, J.; Wen, Z.X.; Yue, Z.F. Numerical Simulation on the Creep Damage Evolution of Nickel-Based Single Crystal Specimens with Slant-Angled Film Cooling Holes. *Rare Met. Mater. Eng.* **2015**, *44*, 2656–2660.

37. Wen, Z.X.; Zhang, D.X.; Li, S.W.; Yue, Z.F.; Gao, J.Y. Anisotropic creep damage and fracture mechanism of nickel-base single crystal superalloy under multiaxial stress. *J. Alloys Compd.* **2016**, *692*, 301–312.

38. Liu, Y.; Peng, Z.F. Estimation of structural volume fraction of phase and relationship between phase amounts in multi-phase alloys. *Acta Metall. Sin.* **2003**, *39*, 22–26.

39. Taylor, G.I.; Elam, C.F. The Plastic Extension and Fracture of Aluminium Crystals. *Proc. R. Soc. Lond.* **1925**, *108*, 25–28.

40. *Abaqus,* version 6.4; Users Manual; ABAQUS Inc.: Pawtucket, RI, USA, 2004.

41. Yin, Z.Y.; Yue, Z.F.; Yang, Z.G.; Cheng, X.M. *Strength and Life Analysis of Nickel-Based Single Crystal Superalloys*; Defense Industry Press: Beijing, China, 2003.